PHYSICS

Probing charge pumping and relaxation of the chiral anomaly in a Dirac semimetal

Bing Cheng[1], Timo Schumann[2], Susanne Stemmer[2], N. P. Armitage[1]*

The linear band crossings of 3D Dirac and Weyl semimetals are characterized by a charge chirality, the parallel or antiparallel locking of electron spin to its momentum. These materials are believed to exhibit an E · B chiral magnetic effect that is associated with the near conservation of chiral charge. Here, we use magneto-terahertz spectroscopy to study epitaxial Cd_3As_2 films and extract their conductivities σ(ω) as a function of E · B. As field is applied, we observe a markedly sharp Drude response that rises out of the broader background. Its appearance is a definitive signature of a new transport channel and consistent with the chiral response, with its spectral weight a measure of the net chiral charge and width a measure of the scattering rate between chiral species. The field independence of the chiral relaxation establishes that it is set by the approximate conservation of the isospin that labels the crystalline point-group representations.

INTRODUCTION

Some of the most remarkable demonstrations of topological states of matter come through their response to electromagnetic fields. Quantum Hall systems show quantized Hall resistances that are precise to better than one part in a billion (*1*), and topological insulators are characterized by a quantized magnetoelectric effect (*2*–*5*). Weyl (WSM) and Dirac semimetals (DSM) are states of matter in which conduction and valence bands touch and disperse linearly around pairs of nodes in momentum space (*6*–*13*). Each node is distinguished by its chirality, i.e., whether the spin of a massless (linearly dispersing) particle is oriented parallel or antiparallel to its momentum. Roughly speaking, Dirac systems can be considered as two copies of Weyl systems, where at each node there are two sets of the linearly dispersing bands with opposite chiral charge. The copies are distinguished by a point-group index or isospin degree of freedom (⇑, ⇓) that labels the crystalline point-group representations (*14*, *15*). These fourfold degenerate three-dimensional (3D) linear band crossings in DSMs are protected by lattice point-group symmetries and are stable as long as the symmetries are respected. The quasi-particles near the touching points can be described by the relativistic Dirac Hamiltonian, $H = \eta v_F \sigma \cdot (k \pm K_D)$, where $\eta = \pm 1$ represents the chirality degree of freedom and $\pm K_D$ represent the valley degrees of freedom and location of the Dirac nodes along a high symmetry direction in momentum space (*14*, *16*).

Despite being essentially metals, WSMs and DSMs can show distinct transport effects that are associated with the near conservation of chiral charge. Unlike the quantum Hall effect, this "chiral anomaly" exists in both the quantum and semiclassical transport limits (*8*, *15*, *17*, *18*, *19*). The phenomenon requires two important ingredients. In the semiclassical limit, the first is a magnetic field–induced coupling between the chiral and the total charge densities via Berry curvature. This aspect is generic to systems with large Berry curvature. The second is a nearly conserved chiral charge, which is a property unique to WSM and DSM systems. The chiral charge is not exactly conserved in any real material, as the chiral symmetry is always violated by effects like nonlinear band dispersions, but these effects vanish in the low energy limit. Therefore, the near conservation of the chiral charge is due to an emergent low-energy chiral symmetry.

Although the effect exists in both semiclassical and quantum transport regimes (*6*), perhaps the most intuitive understanding of the effect can be achieved in the quantum limit. Consider a magnetic field in the z direction that bridges Dirac nodes separated in k_z. As shown in Fig. 1D, due to the particular properties of massless Dirac fermions, a zeroth Landau level (LL) forms, which connects one valley to the other either above or below E_F depending on the relative direction of the magnetic field and the isospin distribution. With the reasonable assumption (discussed more below) that intervalley and isospin relaxation rates ($1/\tau_v$ and $1/\tau_i$) are slower than the intravalley rates ($1/\tau_n$) under the action of an E · B term, for a particular isospin, charge is pumped from one valley to the other. For the opposite isospin, the sense of pumping between valleys is reversed, but note that because of the connectivity of the nodes of the zeroth LL on isospin, the velocity of the zeroth LL at E_F is always the same in the valley that charge is being pumped into. This results in differences in valley ($\mu_{\Uparrow}^{+k_D} - \mu_{\Uparrow}^{-k_D}$) and isospin ($\mu_{\Uparrow}^{+k_D} - \mu_{\Downarrow}^{+k_D}$) chemical potentials and corresponding valley and isospin currents (*6*). These currents and population imbalances can be relaxed only by the relatively slow scattering between nodes of opposite chirality as compared to the normal intravalley scattering that dominates scattering across a node. Intervalley scattering ($1/\tau_v$) is slower than the normal scattering because of the large momentum transfer between nodes, and inter-isospin scattering ($1/\tau_i$) is suppressed by the same symmetry that protects the degeneracies. We call the larger of $1/\tau_v$ and $1/\tau_i$ the chiral relaxation rate $1/\tau_c$, which controls the buildup of valley charge imbalance. Because the chiral charge is not precisely conserved, i.e., it is pumped under the action of collinear electric and magnetic fields, this effect is referred to as the chiral anomaly.

A net valley or isospin population will lead to a chiral current, which relaxes at the lower rate $1/\tau_c$ than a usual current and hence gives an enhanced dc conductance and negative longitudinal magnetoresistance (NLMR). NLMR has been observed in a number of DSM and WSM systems and was widely interpreted as a consequence of the chiral magnetic effect (*6*). However, NLMR is not uniquely caused by this effect, and it is clear that, at least in the high-mobility WSM system, the measurements were affected by the inhomogeneous

[1]Department of Physics and Astronomy, Johns Hopkins University, Baltimore, MD 21218, USA. [2]Materials Department, University of California, Santa Barbara, Santa Barbara, CA 93106, USA.
*Corresponding author. Email: npa@jhu.edu

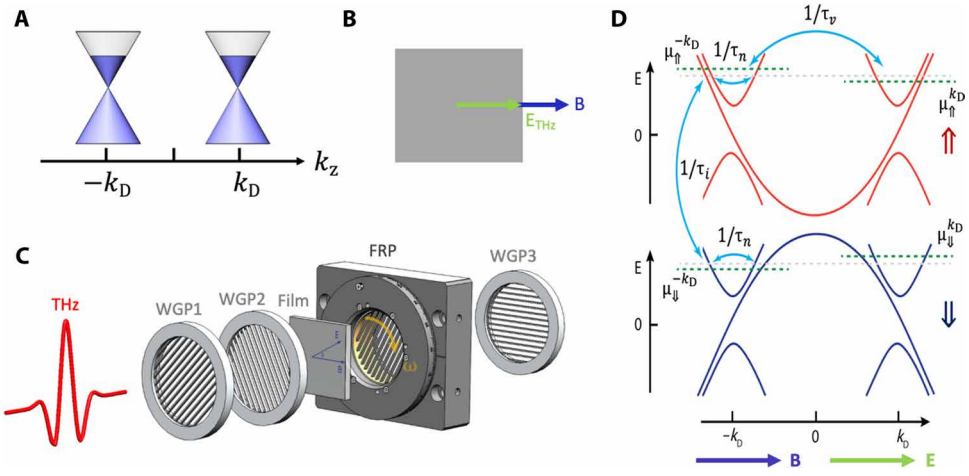

Fig. 1. Charge dynamics of the chiral anomaly in a DSM and the experimental setup. (**A**) Schematic illustration of the low-energy electronic structure of the DSM Cd_3As_2. It hosts two 3D Dirac nodes located along the k_z axis. (**B**) The chiral anomaly is expected when the dc magnetic field and the THz electric field are coaligned. (**C**) Schematic of the time domain magnetoterahertz spectrometer used to collect data. Wire grid polarizer 1 (WGP1) and WGP2 are used to produce linearly polarized terahertz pulse with $E_{THz} \parallel B$ or $E_{THz} \perp B$. A fast rotation polarizer (FRP) is used to modulate terahertz electric field by a frequency near 47 Hz. With WGP3 and lock-in amplifier, the complex transmission matrix can be determined through a single measurement to high precision. (**D**) In a DSM with $E_{THz} \parallel B$, the 3D Dirac states will develop Landau levels (LLs), which are dispersive along the direction of magnetic field. The zeroth LL gives the chiral current. A number of different relaxation rates control the charge dynamics. $1/\tau_n$ is the intranode (normal) scattering rate, $1/\tau_v$ is the intervalley scattering rate, and $1/\tau_i$ is the internode scattering rate at the same momentum valley, but to the other isospin variety.

current flow due to the large transverse magnetoresistances induced by magnetic field, i.e., "current jetting" (*6*, *20*–*23*). In lower-mobility systems, there are other possibilities including mobility fluctuations that may mix Hall and longitudinal responses in sufficiently thick films (*6*, *24*–*26*).

RESULTS AND DISCUSSION

Because of these controversies, experiments that can give conclusive information about the effect are desired (*27*, *28*). As discussed above, a key parameter that governs the chiral anomaly is the chiral relaxation rate $1/\tau_c$. The most convincing way to characterize the intrinsic properties of the chiral anomaly would be to measure $1/\tau_c$ and $1/\tau_n$ directly. To date, most magnetotransport experiments of topological semimetals are performed with dc electric field, for which it is hard to disentangle $1/\tau_c$ and $1/\tau_n$. In this work, we use magneto-terahertz spectroscopy, as shown in Fig. 1C, to study the high-quality epitaxial thin films of DSM Cd_3As_2. Cd_3As_2 is an ideal material for this investigation as it simply presents two quadruply degenerate near-E_F Dirac nodes that sit along the k_z axis that are protected by a C_4 symmetry (Fig. 1A). High-quality (112) oriented Cd_3As_2 films have been grown via molecular beam epitaxy (*29*). Depending on growth parameters, different E_Fs can be achieved (E_F = 46 and 118 meV for samples S1 and S2, respectively; see the Supplementary Materials for these estimates). E_F is generally lower in these films even than in good high single crystals (*30*, *31*). Performing frequency-dependent conductivity experiments offers the opportunity to extract $1/\tau_c$ and $1/\tau_n$ directly. We measured two Cd_3As_2 films and extracted their field-dependent terahertz conductivity. For the films with lower E_F, we found the emergence of a narrow Drude-like peak at low frequency when $E_{THz} \parallel B$. The appearance of this peak in a restricted low-frequency range is the manifestation of a new transport channel. Its systematic dependencies on frequency and field are in precise agreement with expectations of the chiral anomaly and the chiral Drude response in a DSM. An additional advantage of these contactless THz measurements is that they avoid any artifacts associated with inhomogeneous current paths that have plagued dc experiments.

In Fig. 2 (A and B), we show the real part of the THz conductivity at different fields for $E_{THz} \parallel B$ and $E_{THz} \perp B$ for Cd_3As_2 sample S1 (see corresponding σ_2 in the Supplementary Materials) with a low E_F [measured with $B \parallel (\bar{1}10)$]. At zero field, σ_1 is characterized by a Drude-like Lorentzian peak with a scattering rate approximately 1 THz and a 0.7-THz phonon (*32*). As field $B \parallel E_{THz}$ is applied, an additional much sharper Drude-like peak rises out of the zero-field σ_1. That this should be considered a new transport channel with a distinct frequency scale can be seen in that these changes are all at low frequency, i.e., at frequencies above 1 THz, the data do not change. To elaborate this point more clearly, we replot data of Fig. 2A at each frequency as a function of magnetic field in Fig. 3A. One can see that in the low-frequency region (e.g., below 0.4 THz), the THz conductivity steadily increases with magnetic field with a dependence that is approximately B^2 (the expectation for the dc limit of the chiral anomaly). In the high-frequency region (above 1 THz), the increasing trend of THz conductivity becomes negligible, indicating that the chiral anomaly–related transport is confined to the low-frequency region. $B \parallel (\bar{1}\bar{1}2)$ in sample S1 shows a similar effect. This behavior can be contrasted with $E_{THz} \perp B$ that shows a decrease in the low-frequency conductivity over the entire measured spectral range. For this direction, the decreased conductivity is consistent with the usual positive transverse magnetoresistance of conductors in magnetic field. Figure 2A is the major result of this work. As shown in Figs. 2 (C and D) and 3B, another sample S2 measured with $B \parallel (\bar{1}\bar{1}2)$ with a larger E_F shows a similar, though more modest, effect with scattering rates larger than those of S1.

To further demonstrate this result, we plot σ_1 at 0 and 7 T $E_{THz} \parallel B$ and their difference for samples S1 and S2 in Fig. 2 (E and F), respectively.

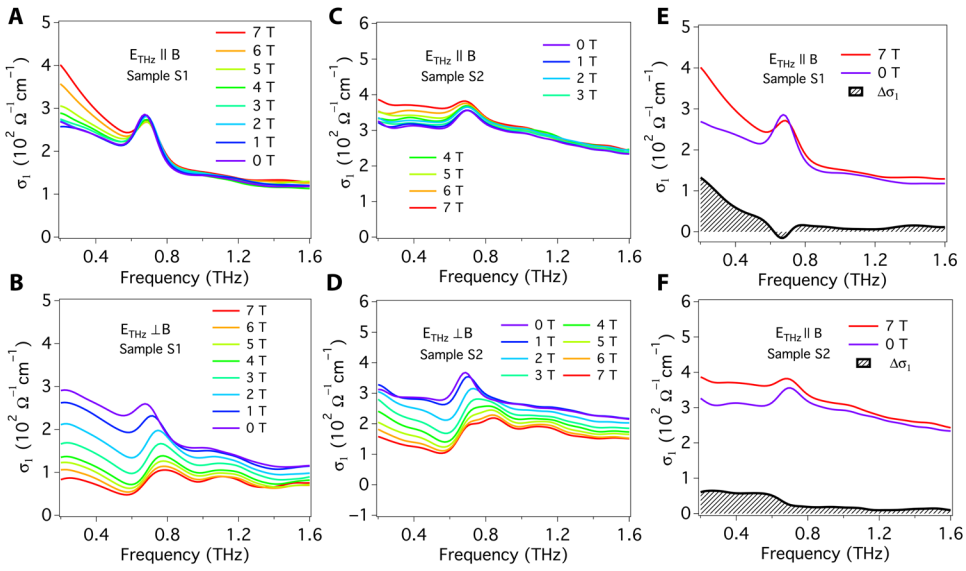

Fig. 2. Terahertz conductivity at different magnetic fields. (**A**) $E_{THz} \parallel B$ with $B \parallel (\bar{1}10)$ for sample S1. Chiral anomaly leads terahertz conductivity σ_1 below 1 THz to be gradually enhanced by magnetic field. (**B**) $E_{THz} \perp B$ with $B \parallel (\bar{1}10)$ for sample S1. The suppression of terahertz conductivity σ_1 is the signature of positive magnetoresistivity, which is generally observed in perpendicular magnetic and electric fields. (**C**) $E_{THz} \parallel B$ for $B \parallel (\bar{1}\bar{1}2)$ sample S2. (**D**) $E_{THz} \perp B$ for $B \parallel (\bar{1}\bar{1}2)$ sample S2. (**E** and **F**) Comparisons of this 0- and 7-T data and their differences for samples S1 and S2. $\Delta\sigma_1$ is the intrinsic chiral conductivity from chiral anomaly. The highlighted gray area represents the strength of charge pumping effect, and its width defines the chiral relaxation rate.

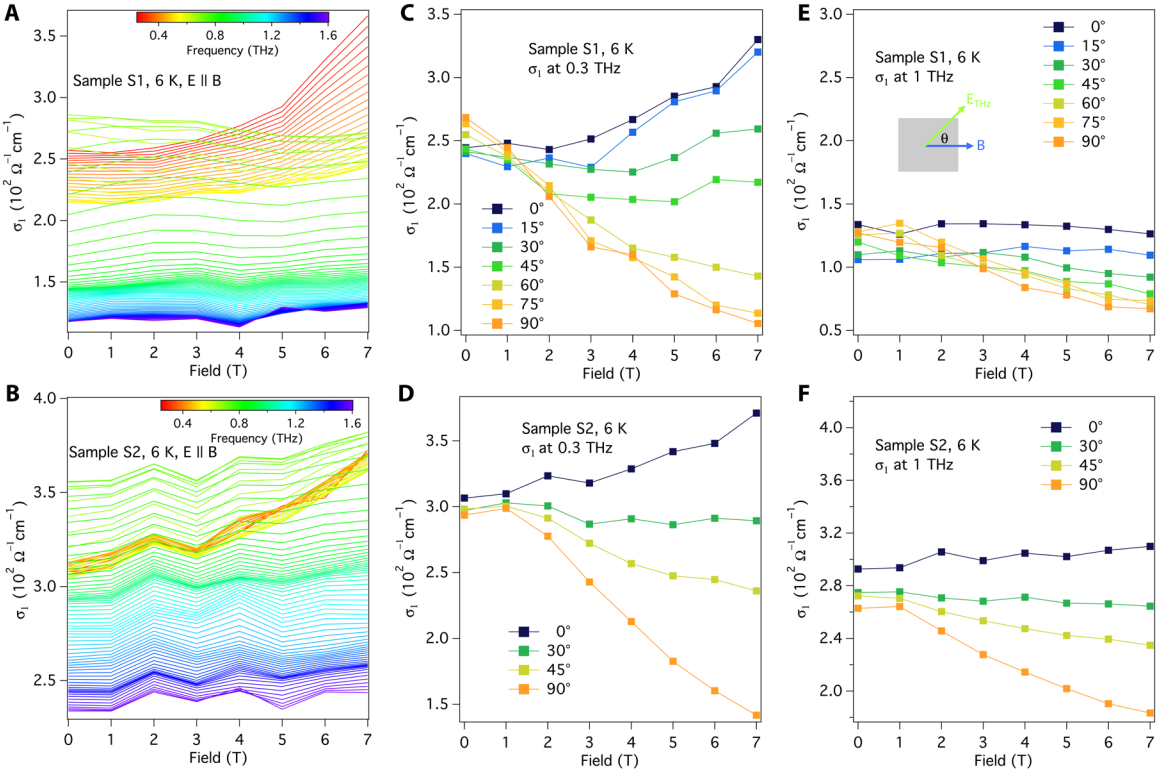

Fig. 3. Terahertz conductivity at different magnetic fields. Terahertz conductivity σ_1 at each frequency (see color bar scale) as a function of magnetic field of (**A**) sample S1 and (**B**) sample S2 with $E_{THz} \parallel B$. Terahertz conductivity (at 0.3 THz) as a function of magnetic field under different terahertz polarization angles of (**C**) sample S1 and (**D**) sample S2. The configuration of polarization angle θ between terahertz electric field and magnetic field is shown by the schematic in (E). Terahertz conductivity (at 1 THz) as a function of magnetic field under different terahertz polarization angles of (**E**) sample S1 and (**F**) sample S2. All data were taken at 6 K.

One can see that, comparing 0 and 7 T, σ_1 contains an emergent sharper Drude response. The difference in these curves, $\Delta\sigma_1 = \sigma_1(B) - \sigma_1(0)$ at 7 T, reveals a narrower zero-frequency peak that characterizes a new transport channel. There are also small changes to the phonon that will be discussed elsewhere.

In Fig. 3 (C and E), we show the conductivity at 0.3 and 1 THz of sample S1 plotted as a function of field with several different terahertz polarization angles. One can see that only the low-frequency data (0.3 THz) shows an enhancement of the conductivity, with the effect being most pronounced when $E \cdot B$ is large. For crossed E and B fields, the magneto-conductivity is negative. Intermediate angles show an effect in between. Similar data are shown for sample S2 in Fig. 3 (D and F). As shown in figs. S10 and S12, the polarization dependence of terahertz conductivity in both samples shows the explicit $\cos^2\theta$ dependence, consistent with the expectation for the chiral anomaly.

Figure 4 (A to D) shows that Drude/Drude-Lorentz oscillator fits to the data that characterize the $E_{THz} \parallel B$ response. Fit details are given in Materials and Methods and fig. S3. In the displayed spectral range, the zero-field spectra are fit well by a single Drude feature and Drude-Lorentz oscillator for the 0.7-THz phonon. The square of the plasma frequency ($\omega_p^2 = Ne^2/\epsilon m$) is related to the spectral weight of a spectral feature in the conductivity. At slightly higher frequencies, there is an overdamped phonon (*32*, *33*) that we incorporate through a broad oscillator centered at 1.7 THz. Small changes in the details of these phonon fits affect none of our main results or conclusions. As field is increased, the new zero-frequency peak emerges and excellent fits can be obtained by the inclusion of an additional sharp Drude term (of width $1/2\pi\tau_c$) with imperceptible changes to the spectral weight and widths of the broader Drude and phonon terms. The fitting parameters as a function of field are shown in Fig. 4 (E and F). For both samples, one can see that the plasma frequencies ω_{pn} and scattering rates $1/2\pi\tau_n$ of the broad Drude oscillator do not have appreciable field evolution. In contrast, the plasma frequencies ω_{pc} of the sharper Drude oscillator increase approximately linearly as a function of magnetic field in both samples. In both samples, $1/2\pi\tau_c$ is approximately one-fourth of $1/2\pi\tau_n$.

This field-induced effect is remarkable, and its origin should be carefully considered. Because of the fact that it is an enhancement of only the low-frequency conductivity, it should not be considered due to either a change in the normal scattering rate itself or change in carrier density, but instead the appearance of a parallel transport channel with a new frequency scale. Moreover, that the part of the spectra associated with the zero-field Drude does not change shows that the effect is not to be associated with effects like spin-dependent scattering (*34*) that would manifest as an overall change in scattering rate. We should also reiterate that an advantage of our contactless THz measurements is that they avoid the artifacts associated with inhomogeneous current paths that occur in very anisotropic conductors when dc currents are applied or in systems with mobility fluctuations (*6*, *20*, *23*–*25*). That the changes to the spectrum are intrinsic is corroborated by the fact that the phonon's spectral weight (Fig. 5B) decreases as the low-frequency conductivity increases (presumably because of increased screening).

In contrast, the appearance of an additional transport channel and new time scale is precisely in agreement with theoretical expectations for the chiral anomaly. In particular, Burkov showed that with increasing magnetic field, an additional Lorentzian-like peak should emerge, the width of which corresponds to the internode scattering rate (*17*). Within this picture, the broader Drude represents the normal intraband transitions inside each Weyl cone, whereas the narrow Drude is evidence for the chiral transport channel, with its spectral weight a direct measure of the chiral population and its width the rate of chiral relaxation $1/2\pi\tau_c$. The fact that $1/2\pi\tau_c$ shows little field dependence is consistent with predictions. It is important to point out here that despite the fact that the $(\bar{1}10)$ and $(\bar{1}\bar{1}2)$ fields break the C_4 symmetry that protects the Dirac nodes, the chiral anomaly is retained. For instance, as discussed in (*35*), a $(\bar{1}10)$ field

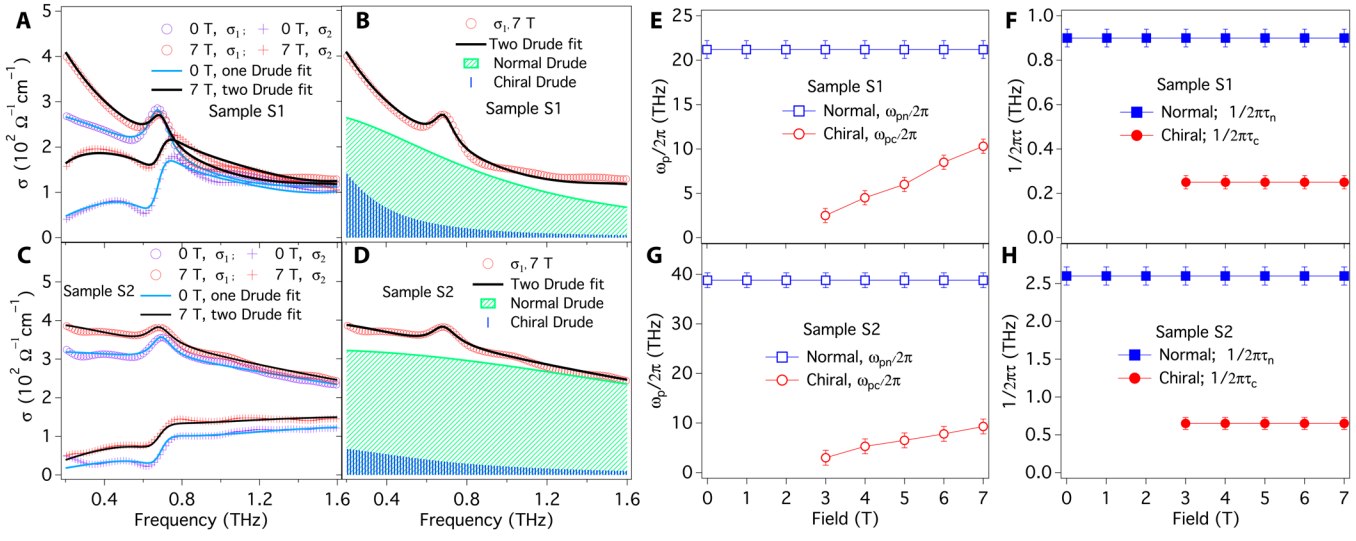

Fig. 4. Dynamical charge pumping and relaxation of the chiral anomaly extracted by Drude-Lorentz fits. (**A** and **B**) Fits to terahertz conductivity of sample S1 with $E_{THz} \parallel B$. The sharper Drude oscillator (blue shadowed area) represents the new transport channel from chiral anomaly. (**C** and **D**) Fits to terahertz conductivity of sample S2 with $E_{THz} \parallel B$. Field-dependent Drude plasma frequency in sample S1 (**E**) and sample S2 (**G**). The plasma frequencies of chiral transport channel ($\omega_{pc}/2\pi$, red) directly correspond to chiral charge pumping and are linear functions of field. Scattering rates in sample S1 (**F**) and sample S2 (**H**). The chiral scattering rates ($1/2\pi\tau_c$, red) control the dynamical process of chiral anomaly as shown in Fig. 1D, and in both samples, they are much smaller than normal bulk scattering rates ($1/2\pi\tau_n$, blue).

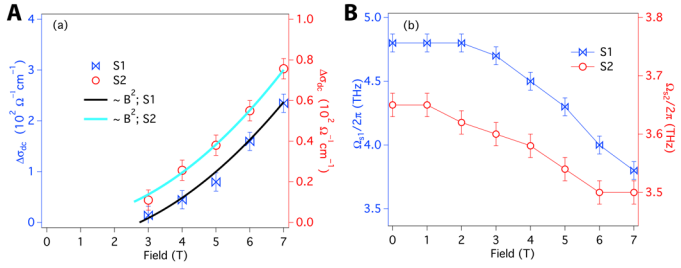

Fig. 5. Intrinsic dc chiral conductivity extrapolated from terahertz conductivity. (**A**) Intrinsic dc magnetoconductivity from chiral anomaly in sample S1 (blue) and sample S2 (red). In both samples, Δσ follows B^2, consistent with the prediction of field dependence of chiral current in semiclassical transport regime. (**B**) Phonon oscillator strength in sample S1 (blue) and sample S2 (red). The oscillator strengths in both samples decrease as the chiral conductivity is enhanced by magnetic field.

(and other fields that preserve a mirror symmetry) results in a line node that is connected to the other valley via a zeroth LL. For other directions, Weyl nodes are generically expected. For instance, a (001) field separates Dirac nodes into Weyl nodes along the z axis but does not cause gapping due to the protection by C_4. Then, deviations of the field from (001) do not cause gaps to form because Weyl nodes are topological objects (*35*). Moreover, even with the accepted large g factor of 16 (*25*), one gets a Zeeman energy of only 3.25 meV. As this is small compared to the Fermi energy, it does not cause appreciable chiral mixing. Please see further discussion on this and related points in the Supplementary Materials.

Through simulations of the Drude responses, we can extrapolate the field-induced conductivity $\Delta\sigma_1(B)$ at zero frequency. Furthermore, $\Delta\sigma_1(B)$ should be equal to the intrinsic dc longitudinal magneto conductivity. In Fig. 5A, we show the extrapolated $\Delta\sigma_1(B)$ of both samples. One can see that above 3 T, $\Delta\sigma_1(B)$ shows a typical B^2 dependence, which is also consistent with the theoretical prediction of the magnetic field dependence of chiral current in the semiclassical transport regime. Note that the small effective negative offset in the B^2 fit for sample S1 may be caused by weak anti-localization at small fields as seen in (*26*).

Chiral transport occurs via a buildup of the effective chiral electrochemical potential through the balance between chiral pumping and internode scattering. However, to distinguish a steady-state chiral current, the chiral scattering rate $1/\tau_c$ must be much smaller than $1/\tau_n$. We find that $1/\tau_c$ is approximately one-fourth of $1/\tau_n$ in both samples. We can compare this relative size of $1/\tau_c$ to $1/\tau_n$ in light of prevailing theory. As mentioned above and shown in Fig. 1D, there are two potential sources of this scattering. Charge can undergo large momentum intervalley scattering ($1/\tau_v$) or can scatter between isospin species at the same valley ($1/\tau_i$). The larger of these determines $1/\tau_c$. Their relative scales to $1/\tau_n$ can, in principle, be determined from band structure parameters.

As discussed in the Supplementary Materials and in (*15*), within a Fermi's golden rule approach and for $k_F \ll K_D$, the intervalley scattering rate can be expressed as $\frac{1}{\tau_n}\left(\frac{k_F}{2K_D}\right)$. There is considerable uncertainty in band structure parameters, but available data (*36*) suggest that K_D is found approximately one-third of the way toward Z along the $\Gamma - Z$ line, i.e., at approximately 0.04 ± 0.01 Å^{-1}. Through analysis of the Drude spectral weight and cyclotron mass of S1, one can estimate a Fermi wave vector k_F of 0.0135 Å^{-1}, which gives $1/\tau_v = 0.0008\ 1/\tau_n$. This is much smaller than observed. The isospin intravalley scattering $1/\tau_i$ is suppressed if the band dispersions are completely linear. However, in a real material, the actual band dispersions will inevitably have quadratic curvature. This quadratic correction mixes chiralities and introduces weak scattering between nodes (see the Supplementary Materials for further discussion). We make an approximation that the impurity potential is spherically symmetric and smooth on the scale of a unit cell and ignore the angular anisotropy of the Fermi wave vector and velocity (v_F); $1/\tau_i$ can be estimated to be $\tau_n^{-1}\left(\frac{B_3 K_D k_F}{2 v_F}\right)^2$ (*15*), which can be expressed in terms of the cyclotron mass m^* as $1/\tau_i = \frac{1}{\tau_n}\left(\frac{B_3 K_D m^*}{2\hbar^2}\right)^2$. A cyclotron mass of $m^* = 0.03 m_e$ was determined in our previous work (*32*), and an upper bound of $B_3 K_D = 30 \pm 15$ eV·Å^2 can be determined from angle-resolved photoemission spectroscopy data (see the Supplementary Materials). This gives $1/\tau_i = 0.0035\ 1/\tau_n$, which as expected for a DSM is larger than $1/\tau_v$, but still much smaller than the $1/\tau_c$ observed. It may be that impurity potentials that break inversion symmetry and couple chiral sectors at order k need to be considered. This should be an area of future study. Recent nonlinear THz experiments have been interpreted in terms of a chiral relaxation rate in the WSM TaAs that is slower than 1 GHz (*28*). Such a slow rate could be due to the much larger separation of nodes in TaAs and/or the lack of isospin scattering.

In this work, we have observed an anomalous THz magnetoconductivity effect in the DSM Cd_3As_2. The effect depends on the relative alignment of the in-plane fields as E · B. This dependence and the evolution of the functional form of the conductivity are in precise agreement with the theory of the chiral anomaly. The finite frequency measurements allow the measurement of a new frequency scale that can be associated with the chiral scattering rate. What is not in precise agreement with prevailing theory are the relative scales of the chiral scattering rate and intranode scattering, as we find the chiral scattering much stronger than predicted. This raises questions about the nature of charge transport in the DSM and chiral scattering. It may be that accepted aspects of the band structure need to be revised (*37*) or that more realistic models of impurity scattering need to be developed.

MATERIALS AND METHODS

Film growth

A number of 112 oriented Cd3As2 films were grown by molecular beam epitaxy on (111)B GaAs substrates. Samples S1 and S2 have thickness of 280 and 300 nm, respectively. Further details of the film growth can be found elsewhere (*29*). The dc magneto transport of both films is similar to the previous work on the films of this DSM (*26*).

Experimental setup

In time domain terahertz spectroscopy, an 800-nm femtosecond laser pulse is split along two paths and sequentially excites a pair of photoconductive Auston-switch antennae. A broadband THz range pulse is emitted by one antenna, transmitted through the sample under test, and measured at the other antenna by sampling with the split-off pulse. By varying the length difference between the two paths, the time dependence of the electric field is measured. The time domain trace is then Fourier-transformed into the frequency domain. Taking the ratio of the transmission through a sample to that of a reference resolves the full complex transmission coefficient. A closed-cycle 7-T superconducting magnet is used to measure

field-dependent terahertz responses. Samples can be measured with the field direction perpendicular (Voigt geometry) or parallel (Faraday geometry) to the light wave vector (*38*). In the current case of thin films deposited on top of an insulating substrate, the transmission can be inverted to obtain the complex conductivity by using the appropriate expression in the thin-film approximation (*39*).

Drude-Lorentz fits

To find the scattering rate and spectral weight of the lowest frequency features, the optical conductivity data were fit to a modified Drude/Drude-Lorentz model. We use one Drude oscillator to account for the normal Drude transport of Dirac fermions and the other to account for the chiral Drude response. The expression is

$$\sigma(\omega) = \epsilon_0 \left[-\frac{\omega_{\mathrm{pn}}^2}{i\omega - 1/\tau_n} - \frac{\omega_{\mathrm{pc}}^2}{i\omega - 1/\tau_c} - \frac{i\omega\Omega_s^2}{\omega_0^2 - \omega^2 - i/\tau_0} - i(\epsilon_\infty - 1)\omega \right] \quad (1)$$

Here, $1/2\pi\tau_n$ is the intranode (normal) scattering rate of the normal Drude term and $1/2\pi\tau_c$ is the internode (chiral) scattering rate of the field-induced Drude term. ω_{pn} and ω_{pc} are their plasma frequencies. Ω_s is the phonon's oscillator strength, ω_0 is the central frequency, and $1/2\pi\tau_0$ is the linewidth. The background polarizability ϵ_∞ originates from absorptions above the measured spectral range including phonons and interband absorptions.

SUPPLEMENTARY MATERIALS

Supplementary material for this article is available at http://advances.sciencemag.org/cgi/content/full/7/16/eabg0914/DC1

REFERENCES AND NOTES

1. K. v. Klitzing, G. Dorda, M. Pepper, New method for high-accuracy determination of the fine-structure constant based on quantized Hall resistance. *Phys. Rev. Lett.* **45**, 494–497 (1980).
2. X.-L. Qi, T. L. Hughes, S.-C. Zhang, Topological field theory of time-reversal invariant insulators. *Phys. Rev. B* **78**, 195424 (2008).
3. A. M. Essin, J. E. Moore, D. Vanderbilt, Magnetoelectric polarizability and axion electrodynamics in crystalline insulators. *Phys. Rev. Lett.* **102**, 146805 (2009).
4. L. Wu, M. Salehi, N. Koirala, J. Moon, S. Oh, N. P. Armitage, Quantized Faraday and Kerr rotation and axion electrodynamics of a 3D topological insulator. *Science* **354**, 1124–1127 (2016).
5. N. P. Armitage, L. Wu, On the matter of topological insulators as magnetoelectrics. *SciPost Phys.* **6**, 046 (2019).
6. N. P. Armitage, E. J. Mele, A. Vishwanath, Weyl and Dirac semimetals in three-dimensional solids. *Rev. Mod. Phys.* **90**, 015001 (2018).
7. A. A. Abrikosov, S. D. Beneslavskii, Possible existence of substances intermediate between metals and dielectrics. *JETP* **32**, 699 (1970).
8. H. B. Nielsen, M. Ninomiya, The Adler-Bell-Jackiw anomaly and Weyl fermions in a crystal. *Phys. Lett. B* **130**, 389–396 (1983).
9. G. E. Volovik, *The Universe in a Helium Droplet* (Oxford Univ. Press, 2003).
10. S. Murakami, Phase transition between the quantum spin Hall and insulator phases in 3D: Emergence of a topological gapless phase. *New J. Phys.* **9**, 356 (2007).
11. X. Wan, A. M. Turner, A. Vishwanath, S. Y. Savrasov, Topological semimetal and Fermi-arc surface states in the electronic structure of pyrochlore iridates. *Phys. Rev. B* **83**, 205101 (2011).
12. K.-Y. Yang, Y.-M. Lu, Y. Ran, Quantum Hall effects in a Weyl semimetal: Possible application in pyrochlore iridates. *Phys. Rev. B* **84**, 075129 (2011).
13. S. M. Young, S. Zaheer, J. C. Y. Teo, C. L. Kane, E. J. Mele, A. M. Rappe, Dirac semimetal in three dimensions. *Phys. Rev. Lett.* **108**, 140405 (2012).
14. Z. Wang, H. Weng, Q. Wu, X. Dai, Z. Fang, Three-dimensional Dirac semimetal and quantum transport in Cd_3As_2. *Phys. Rev. B* **88**, 125427 (2013).
15. S. A. Parameswaran, T. Grover, D. A. Abanin, D. A. Pesin, A. Vishwanath, Probing the chiral anomaly with nonlocal transport in three-dimensional topological semimetals. *Phys. Rev. X* **4**, 031035 (2014).
16. Z. Wang, Y. Sun, X.-Q. Chen, C. Franchini, G. Xu, H. Weng, X. Dai, Z. Fang, Dirac semimetal and topological phase transitions in A_3Bi (A=Na, K, Rb). *Phys. Rev. B* **85**, 195320 (2012).
17. A. A. Burkov, Dynamical density response and optical conductivity in topological metals. *Phys. Rev. B* **98**, 165123 (2018).
18. D. T. Son, B. Z. Spivak, Chiral anomaly and classical negative magnetoresistance of Weyl metals. *Phys. Rev. B* **88**, 104412 (2013).
19. A. A. Burkov, Negative longitudinal magnetoresistance in Dirac and Weyl metals. *Phys. Rev. B* **91**, 245157 (2015).
20. F. Arnold, C. Shekhar, S. C. Wu, Y. Sun, R. D. dos Reis, N. Kumar, M. Naumann, M. O. Ajeesh, M. Schmidt, A. G. Grushin, J. H. Bardarson, M. Baenitz, D. Sokolov, H. Borrmann, M. Nicklas, C. Felser, E. Hassinger, B. Yan, Negative magnetoresistance without well-defined chirality in the Weyl semimetal TaP. *Nat. Commun.* **7**, 11615 (2016).
21. A. B. Pippard, *Magnetoresistance in Metals* (Cambridge Univ. Press, 1989).
22. R. D. dos Reis, M. O. Ajeesh, N. Kumar, F. Arnold, C. Shekhar, M. Naumann, M. Schmidt, M. Nicklas, E. Hassinger, On the search for the chiral anomaly in Weyl semimetals: The negative longitudinal magnetoresistance. *New J. Phys.* **18**, 085006 (2016).
23. S. Liang, J. Lin, S. Kushwaha, J. Xing, N. Ni, R. J. Cava, N. P. Ong, Experimental tests of the chiral anomaly magnetoresistance in the Dirac-Weyl semimetals Na_3Bi and GdPtBi. *Phys. Rev. X* **8**, 031002 (2018).
24. M. M. Parish, P. B. Littlewood, Non-saturating magnetoresistance in heavily disordered semiconductors. *Nature* **426**, 162–165 (2003).
25. A. Narayanan, M. D. Watson, S. F. Blake, N. Bruyant, L. Drigo, Y. L. Chen, D. Prabhakaran, B. Yan, C. Felser, T. Kong, P. C. Canfield, A. I. Coldea, Linear magnetoresistance caused by mobility fluctuations in *n*-doped Cd_3As_2. *Phys. Rev. Lett.* **114**, 117201 (2015).
26. T. Schumann, M. Goyal, D. A. Kealhofer, S. Stemmer, Negative magnetoresistance due to conductivity fluctuations in films of the topological semimetal Cd_3As_2. *Phys. Rev. B* **95**, 241113 (2017).
27. A. L. Levy, A. B. Sushkov, F. Liu, B. Shen, N. Ni, H. D. Drew, G. S. Jenkins, Optical evidence of the chiral magnetic anomaly in the Weyl semimetal TaAs. *Phys. Rev. B* **101**, 125102 (2020).
28. M. M. Jadidi, M. Kargarian, M. Mittendorff, Y. Aytac, B. Shen, J. C. Knig-Otto, S. Winnerl, N. Ni, A. L. Gaeta, T. E. Murphy, H. D. Drew, Nonlinear optical control of chiral charge pumping in a topological Weyl semimetal. *Phys. Rev. B* **102**, 245123 (2020).
29. T. Schumann, M. Goyal, H. Kim, S. Stemmer, Molecular beam epitaxy of Cd_3As_2 on a III-V substrate. *APL Mater.* **4**, 126110 (2016).
30. A. Akrap, M. Hakl, S. Tchoumakov, I. Crassee, J. Kuba, M. O. Goerbig, C. C. Homes, O. Caha, J. Novk, F. Teppe, W. Desrat, S. Koohpayeh, L. Wu, N. P. Armitage, A. Nateprov, E. Arushanov, Q. D. Gibson, R. J. Cava, D. van der Marel, B. A. Piot, C. Faugeras, G. Martinez, M. Potemski, M. Orlita, Magneto-optical signature of massless Kane electrons in Cd_3As_2. *Phys. Rev. Lett.* **117**, 136401 (2016).
31. D. Neubauer, J. P. Carbotte, A. A. Nateprov, A. Lhle, M. Dressel, A. V. Pronin, Interband optical conductivity of the [001]-oriented Dirac semimetal Cd_3As_2. *Phys. Rev. B* **93**, 121202 (2016).
32. B. Cheng, T. Schumann, Y. Wang, X. Zhang, D. Barbalas, S. Stemmer, N. P. Armitage, A large effective phonon magnetic moment in a Dirac semimetal. *Nano Lett.* **8**, 5991–5996 (2020).
33. S. Yue, H. T. Chorsi, M. Goyal, T. Schumann, R. Yang, T. Xu, B. Deng, S. Stemmer, J. A. Schuller, B. Liao, Soft phonons and ultralow lattice thermal conductivity in the Dirac semimetal Cd_3As_2. *Phys. Rev. Res.* **1**, 033101 (2019).
34. R. P. van Gorkom, J. Caro, T. M. Klapwijk, S. Radelaar, Temperature and angular dependence of the anisotropic magnetoresistance in epitaxial Fe films. *Phys. Rev. B* **63**, 134432 (2001).
35. J. Cano, B. Bradlyn, Z. Wang, M. Hirschberger, N. P. Ong, B. A. Bernevig, Chiral anomaly factory: Creating Weyl fermions with a magnetic field. *Phys. Rev. B* **95**, 161306 (2017).
36. S. Borisenko, Q. Gibson, D. Evtushinsky, V. Zabolotnyy, B. Bchner, R. J. Cava, Experimental realization of a three-dimensional Dirac semimetal. *Phys. Rev. Lett.* **113**, 027603 (2014).
37. S. Roth, H. Lee, A. Sterzi, M. Zacchigna, A. Politano, R. Sankar, F. C. Chou, G. Di Santo, L. Petaccia, O. V. Yazyev, A. Crepaldi, Reinvestigating the surface and bulk electronic properties of Cd_3As_2. *Phys. Rev. B* **97**, 165439 (2018).
38. E. Palik, J. Furdyna, Infrared and microwave magnetoplasma effects in semiconductors. *Rep. Prog. Phys.* **33**, 1193–1322 (1970).
39. B. Cheng, L. Wu, N. J. Laurita, H. Singh, M. Chand, P. Raychaudhuri, N. P. Armitage, Anomalous gap-edge dissipation in disordered superconductors on the brink of localization. *Phys. Rev. B* **93**, 180511(R) (2016).
40. M. Hirschberger, S. Kushwaha, Z. Wang, Q. Gibson, S. Liang, C. A. Belvin, B. A. Bernevig, R. J. Cava, N. P. Ong, The chiral anomaly and thermopower of Weyl fermions in the half-Heusler GdPtBi. *Nat. Mater.* **15**, 1161–1165 (2016).
41. X. Huang, L. Zhao, Y. Long, P. Wang, D. Chen, Z. Yang, H. Liang, M. Xue, H. Weng, Z. Fang, X. Dai, G. Chen, Observation of the chiral-anomaly-induced negative magnetoresistance in 3D Weyl semimetal TaAs. *Phys. Rev. X* **5**, 031023 (2015).
42. Q. Li, D. E. Kharzeev, C. Zhang, Y. Huang, I. Pletikosić, A. V. Fedorov, R. D. Zhong, J. A. Schneeloch, G. D. Gu, T. Valla, Chiral magnetic effect in $ZrTe_5$. *Nat. Phys.* **15**, 550–554 (2015).

43. T. Higo, H. Man, D. B. Gopman, L. Wu, T. Koretsune, O. M. J. van t Erve, Y. P. Kabanov, D. Rees, Y. Li, M.-T. Suzuki, S. Patankar, M. Ikhlas, C. L. Chien, R. Arita, R. D. Shull, J. Orenstein, S. Nakatsuji, Large magneto-optical Kerr effect and imaging of magnetic octupole domains in an antiferromagnetic metal. *Nat. Photon.* **12**, 73–78 (2018).
44. L. Wu, W.-K. Tse, M. Brahlek, C. M. Morris, R. V. Aguilar, N. Koirala, S. Oh, N. P. Armitage, High-resolution faraday rotation and electron-phonon coupling in surface states of the bulk-insulating topological insulator $Cu_{0.02}Bi_2Se_3$. *Phys. Rev. Lett.* **115**, 217602 (2015).
45. B. Cheng, P. Taylor, P. Folkes, C. Rong, N. P. Armitage, Magnetoterahertz response and faraday rotation from massive Dirac fermions in the topological crystalline insulator $Pb_{0.5}Sn_{0.5}Te$. *Phys. Rev. Lett.* **122**, 097401 (2019).
46. S. Nandy, G. Sharma, A. Taraphder, S. Tewari, Chiral anomaly as the origin of the planar Hall effect in Weyl semimetals. *Phys. Rev. Lett.* **119**, 176804 (2017).
47. A. A. Burkov, Giant planar Hall effect in topological metals. *Phys. Rev. B* **96**, 041110 (2017).
48. B. Plenkiewicz, P. R. Wallace, P. Plenkiewicz, The role of vacancies in the band structure of Cd_3As_2. *Solid State Commun.* **50**, 681–684 (1984).
49. E. O. Kane, Band structure of indium antimonide. *J. Phys. Chem. Solid* **1**, 249–261 (1957).
50. M. Neupane, S.-Y. Xu, R. Sankar, N. Alidoust, G. Bian, C. Liu, I. Belopolski, T.-R. Chang, H.-T. Jeng, H. Lin, A. Bansil, F. Chou, M. Z. Hasan, Observation of a topological 3D Dirac semimetal phase in high-mobility Cd_3As_2. *Nat. Commun.* **5**, 3786 (2014).

Acknowledgments: We would like to thank S. Borisenko, A. Burkov, J. Cano, X. Dai, D. Kharzeev, S. Parameswaran, M. Parish, J. Pixley, and A. Vishwanath for helpful discussions. **Funding:** Experiments at JHU were supported by ARO grant W911NF-15-1-0560 and ARO MURI W911NF2020166 "Implementation of Axion Electrodynamics in Topological Films and Devices." Work at UCSB was supported by the Vannevar Bush Faculty Fellowship program by the U.S. Department of Defense (grant no. N00014-16-1-2814). **Author contributions:** B.C. and N.P.A. conceived the project. B.C. performed and analyzed the time domain magneto terahertz spectroscopy measurements and data. Films were developed by T.S. and S.S. T.S. performed dc transport measurements. The manuscript was written by B.C. and N.P.A. with input from all authors. **Competing interests:** The authors declare that they have no competing interests. **Data and materials availability:** All data needed to evaluate the conclusions in the paper are present in the paper and/or the Supplementary Materials. Additional data related to this paper may be requested from the authors.

Submitted 9 December 2020
Accepted 1 March 2021
Published 16 April 2021
10.1126/sciadv.abg0914

Citation: B. Cheng, T. Schumann, S. Stemmer, N. P. Armitage, Probing charge pumping and relaxation of the chiral anomaly in a Dirac semimetal. *Sci. Adv.* **7**, eabg0914 (2021).